ES-PIM applied to buckling of variable angle tow laminates

Giovani Pereira Castro, Saullo; Donadon, Maurício V. ; Guimarães, Thiago A.M.

DOI
10.1016/j.compstruct.2018.10.058

Publication date
2019

Document Version
Accepted author manuscript

Published in
Composite Structures

ES-PIM applied to Buckling of Variable Angle Tow Laminates

Saullo G. P. Castro [a*]
Maurício V. Donadon [b]
Thiago A. M. Guimarães [c]

[a] *Faculty of Aerospace Engineering, Delft University of Technology, 2629 HS Delft, Netherlands*
[b] *Department of Aeronautical Engineering, ITA – Technological Institute of Aeronautics, 12228-900 São José dos Campos-SP, Brazil.*
[c] *Federal University of Uberlândia, 38408-100 Uberlândia-MG, Brazil*

Abstract

The increasing need for automatic mesh generation has led to the development of efficient triangulation algorithms that are able to discretize any 2D or 3D domain. Modern finite element formulations based on strain smoothing techniques (SFEM) provide enhanced convergence properties, preventing yet the stiffening behavior of triangular meshes. Recent research has shown that meshless methods based on triangular mapping of the integration domain can be used to produce even better convergence properties than SFEM. The present study will explore the Edge-based Smoothed Point Interpolation Method (ES-PIM) as a meshless solution to investigate linear buckling on variable angle tow (VAT) laminates. Such advanced composite structures show a heterogeneous distribution of constitutive properties and thickness, presenting additional challenges to the numerical solution. Important aspects related to the transverse shear correction herein adopted are investigated, leading to interesting conclusions regarding the possibility to use the ES-PIM for conservative estimates of the critical buckling load of VAT laminates.

Keywords: meshless; es-pim; buckling; tow steering; variable angle tow; variable stiffness; composite; strain smoothing

1. Introduction

The finite element method (FEM) is regarded as one of the best methodologies for solving practical problems efficiently in almost all areas of engineering and physical sciences [1]. The only types of finite elements that can be automatically generated for any complex geometries are the triangular and tetrahedral types, which show overly stiff behavior when linear interpolation is used [1,2]. Among the various numerical strategies that tried to solve some of the problems with conventional FEM are: the hybrid FEM techniques [3], for which there is no effective formulation for triangular/tetrahedral elements so far [1]; meshfree methods [2], which have shown a considerable development recently, but yet carry the burden on increased programming efforts and considerably higher computational costs. Smoothed finite element methods (S-FEM) have proven to be a valuable combination of meshfree techniques with the standard FEM.
The strain smoothing technique first proposed by Chen et al.[4] was idealized to solve intrinsic non-local properties of two meshfree methods: Moving Least Squares (MLS) and Reproducing Kernel (RK). Subsequently, Liu et al. [5] extended strain smoothing to finite element formulations, developing shortly after the so called generalized gradient smoothing technique [6]. The success of smoothed finite element methods (SFEM) can be largely perceived from the amount of relevant literature applying SFEM, among others: general shell analysis [7–10], functionally graded composite plates [11–13], optimization of composite laminates [14–16] and fracture mechanics [17,18]. Liu established the G space theory [19] and the weakened weak formulation (W^2) [20] for various types of problems, offering new possibilities for developing a wide new class of compatible and incompatible soft models with distinct properties such as conformability, volumetric locking free, super-convergence, upper and lower bound, and ultra-accuracy [1].

Edge-based smoothed techniques such as the edge-based smoothed point interpolation method – ES-PIM – developed by Liu and his research group [2] have shown a great balance of ultra-convergence, stability and performance, even for highly dynamic analyses [21–26]. Liu et al. [5] have demonstrated the potential of the ES-PIM for efficient error estimations and local remeshing using Delaunay triangulation [2], paving the way for modern adaptive mesh algorithms based on *a posteriori* error estimation, capable of estimating whether a local refinement is required. The refinement is carried out by creating additional interpolation points (nodes) in the background triangular or tetrahedral mesh that represents the domain [2].

VAT laminates have a growing importance due to their superior tailoring potential when compared to conventional laminates with constant ply angles. Recent studies have focused on the development of efficient numerical methods for the analysis and optimization of VAT laminates aiming postbuckling and other nonlinear responses [27–31]. The authors believe that the ES-PIM can be a strong competitor among these numerical tools aiming the design of VAT laminates. Although the capability of the ES-PIM has been proven in many applications, to the authors' knowledge there are no studies demonstrating the effectiveness of the ES-PIM for linear buckling nor its application on the analysis of composite laminates with heterogeneous properties, such as those manufactured variable tow techniques, where variations of thickness and laminae angle take place along the structural domain. The investigation carried out in the present study propose a general interpolation procedure based on a nodal distribution of the constitutive properties that is properly averaged during the strain smoothing operations performed in the ES-PIM.

* Corresponding author. Tel.: +31 6 21 89 33 67
Email address: S.G.P.Castro@tudelft.nl (Saullo G. P. Castro)

The Discrete Shear Gap (DSG) technique, originally proposed by Bletzinger [32], is applied to obtain the transverse shear stiffnesses, adopting the methodology proposed by Nguyen-Xuan et al. [10] and Phung-Van et al. [33] to perform a triangular cell-based smoothing, using corrected transverse shear properties according to Lyly et al. [34]. The present study ends after demonstrating the effectiveness of the ES-PIM for linear buckling of variable stiffness composite shells against NX Nastran's CTRIA3 element [35].

2. Buckling Equations for the ES-PIM

Linear buckling equations for any solid continuum can be derived from the neutral equilibrium criterion [36,37], given in Eq. (1) where W is the total potential energy of the system.

$$\delta^2 W = 0 \tag{1}$$

Using the First-order Shear Deformation Theory (FSDT), the total potential of the 2D continuum Ω bounded by boundary Γ can be represented as:

$$\begin{gathered} W = U + V \\ U = \frac{1}{2}\int_{\Omega} \left(\varepsilon_i^m N_i + \varepsilon_i^b M_i + \varepsilon_i^s Q_i\right) d\Omega \\ V = \int_{\Gamma} u_i \, t_i \, d\Gamma \\ t_i = \sigma_{ij} \, n_j \end{gathered} \tag{2}$$

where: U is the strain energy within Ω; V the external work applied on Γ; t_i is the traction on Γ; n_i the unit outward normal; σ_{ij} the component of the stress tensor; ε_i^m, ε_i^b, ε_i^s are respectively the components of the membrane, bending and transverse shear vectors; N_i, M_i and Q_i are respectively the components of the membrane, bending and transverse distributed force vectors. The strain vectors following Mindlin-Reissner plate theory [38–40] are:

$$\begin{gathered} \boldsymbol{\varepsilon}^m = \begin{Bmatrix} \varepsilon_{xx} \\ \varepsilon_{yy} \\ \gamma_{xy} \end{Bmatrix} = \begin{Bmatrix} u_{,x} + \frac{1}{2} w_{,x}^2 \\ v_{,y} + \frac{1}{2} w_{,y}^2 \\ u_{,y} + v_{,x} + w_{,x}\, w_{,y} \end{Bmatrix} \\ \boldsymbol{\varepsilon}^b = \begin{Bmatrix} \kappa_{xx} \\ \kappa_{yy} \\ \kappa_{xy} \end{Bmatrix} = \begin{Bmatrix} \phi_{x,x} \\ \phi_{y,y} \\ \phi_{x,y} + \phi_{y,x} \end{Bmatrix} \\ \boldsymbol{\varepsilon}^s = \begin{Bmatrix} \gamma_{xz} \\ \gamma_{yz} \end{Bmatrix} = \begin{Bmatrix} w_{,x} + \phi_x \\ w_{,y} + \phi_y \end{Bmatrix} \end{gathered} \tag{3}$$

The second variation of the strain energy and external work can now be computed, assuming small quantities for $\delta^2\left(u, v, w, \phi_x, \phi_y\right)_{,(x,y)} = \delta^2\left(\phi_x, \phi_y\right) = 0$; and no follower traction forces such that $\delta t_i = 0$:

$$\begin{gathered} \delta^2 U = \int_{\Omega} \left(\delta\varepsilon_i^m \delta N_i + \delta w_{,i}\, N_{ij} \delta w_{,j} + \delta\varepsilon_i^b \delta M_i + \delta\varepsilon_i^s \delta Q_i\right) d\Omega \\ \delta^2 V = 0 \end{gathered} \tag{4}$$

with N_{ij} representing the three components of the membrane stress state: N_{xx}, N_{yy} and N_{xy}. Applying the following constitutive relations:

$$\begin{gathered} \delta N_i = A_{ij} \delta\varepsilon_j^m + B_{ij} \delta\varepsilon_j^b \\ \delta M_i = D_{ij} \delta\varepsilon_j^b + B_{ij} \delta\varepsilon_j^m \\ \delta Q_i = E_{ij} \delta\varepsilon_j^s \end{gathered} \tag{5}$$

where A_{ij}, B_{ij}, D_{ij} are calculated using Eq. (6) from the laminae stiffnesses $\bar{Q}_{ij}$ already transformed to the laminate coordinate system [41]. Distances z_{inf_k} and z_{sup_k} are respectively the bottom and top z positions of the k^{th} ply. The transverse shear stiffness terms E_{ij} are defined in Section 2.1 according to the discrete shear gap formulation herein presented, c.f. Eq. (26).

$$\begin{aligned} A_{ij} &= \sum_k \left(z_{sup_k} - z_{inf_k}\right)\bar{Q}_{ij} \\ B_{ij} &= \frac{1}{2}\sum_k \left(z_{sup_k}^2 - z_{inf_k}^2\right)\bar{Q}_{ij} \\ D_{ij} &= \frac{1}{3}\sum_k \left(z_{sup_k}^3 - z_{inf_k}^3\right)\bar{Q}_{ij} \end{aligned} \tag{6}$$

When the ES-PIM is used two types of edges are identified in the background triangular mesh used for integration: interior (a) and boundary (b); as highlighted in Fig. 1. Each highlighted zone of Fig. 1 consists on a subdomain Ω_C such that $\sum \Omega_C = \Omega$ and $\Omega_i \cap \Omega_j = 0$. Thus, using Eqs. (4) and (5), the neutral equilibrium criterion for the discretized system with n sub-domains can be written as:

$$\begin{aligned} \sum_{C=1}^{n} \int_{\Omega_C} \Big(&\delta\varepsilon_{i_C}^{m} A_{ij} \delta\varepsilon_{j_C}^{m} + \delta\varepsilon_{i_C}^{m} B_{ij} \delta\varepsilon_{j_C}^{b} + \delta\varepsilon_{i_C}^{b} B_{ij} \delta\varepsilon_{j_C}^{m} + \delta\varepsilon_{i_C}^{b} D_{ij} \delta\varepsilon_{j_C}^{b} + \\ &+\delta w_{,i_C} N_{ij} \delta w_{,j_C} + \delta\varepsilon_{i_C}^{s} E_{ij} \delta\varepsilon_{j_C}^{s}\Big)\, d\Omega_C = 0 \end{aligned} \tag{7}$$

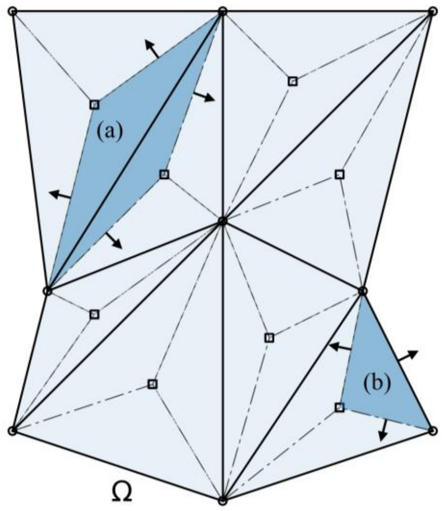

Fig. 1: Integration Cells for (a) Inner Edges and (b) Boundary Edges

A smoothing operator is applied to Eq. (7) with the objective to achieve constant smoothed strain quantities for $\delta\varepsilon_{i_C}^{m}$, $\delta\varepsilon_{i_C}^{b}$, $\delta\varepsilon_{i_C}^{s}$ and constant smoothed quantities for $w_{,i}$ within Ω_C. Representing every partial derivative in Eq. (7) as $f_{,i}$ and the smoothed partial derivatives as $\hat{f}_{,i}$, the smoothing operation for each subdomain Ω_C can be written as [5]:

$$\hat{f}_{,i} = \int_{\Omega_C} f_{,x}\ \Phi\ d\Omega_C \tag{8}$$

where Φ is assumed to be constant within the integration cell Ω_C and null elsewhere [5]:

$$\Phi = \begin{cases} 1/A_C & x \in \Omega_C \\ 0 & x \notin \Omega_C \end{cases} \tag{9}$$

with A_C being the area of Ω_C, i.e. $A_C = \int_{\Omega_C} d\Omega_C$. Applying the divergence theorem [42] to Eq. (8) transforms the area integration of the divergence of a vector field into a boundary integration around the cell contour Γ_C, which can be written as:

$$\hat{f}_{,i} = \frac{1}{A_C} \int_{\Gamma_C} f\, \boldsymbol{n}\, d\Gamma_C \tag{10}$$

where $\mathbf{n} = \{ n_x \quad n_y \}^T$ is the vector normal to the boundary Γ_C; n_x and n_y are its components, as illustrated in Fig. 2. Applying Eq. (10) and keeping only the linear terms, the smoothed membrane $\hat{\boldsymbol{\varepsilon}}_C^m$, bending $\hat{\boldsymbol{\varepsilon}}_C^b$ strain and $\hat{w}_{,i}$; that are constant within Ω_C; can be calculated with an integration over Γ_C:

$$\hat{\boldsymbol{\varepsilon}}_C^m = \frac{1}{A_C} \int_{\Gamma_C} \begin{Bmatrix} n_x u \\ n_y v \\ n_y u + n_x v \end{Bmatrix} d\Gamma_C$$

$$\hat{\boldsymbol{\varepsilon}}_C^b = \frac{1}{A_C} \int_{\Gamma_C} \begin{Bmatrix} n_x \phi_x \\ n_y \phi_y \\ n_y \phi_x + n_x \phi_y \end{Bmatrix} d\Gamma_C \tag{11}$$

$$\begin{Bmatrix} \hat{w}_{,x_C} \\ \hat{w}_{,y_C} \end{Bmatrix} = \frac{1}{A_C} \int_{\Gamma_C} \begin{Bmatrix} n_x w \\ n_y w \end{Bmatrix} d\Gamma_C$$

Note that the transverse shear terms $\varepsilon_{i_C}^s$ of Eq. (7) were not smoothed and therefore not present in Eq. (11). As mentioned earlier, in the present study the transverse shear stiffness is calculated using the discrete shear gap (DSG) method, such that smoothing is applied directly on the DSG results.

For edge-based integration cells built from a background triangular mesh, the boundary integration of Eq. (11) will have 4 straight segments for interior edges, whereas 3 straight segments for boundary edges, as illustrated in Fig. 1 and Fig. 2. Note that using Gauss quadrature rules only one integration point at the middle of each straight segment suffices, since linear interpolation functions for the displacement fields are being used [2].

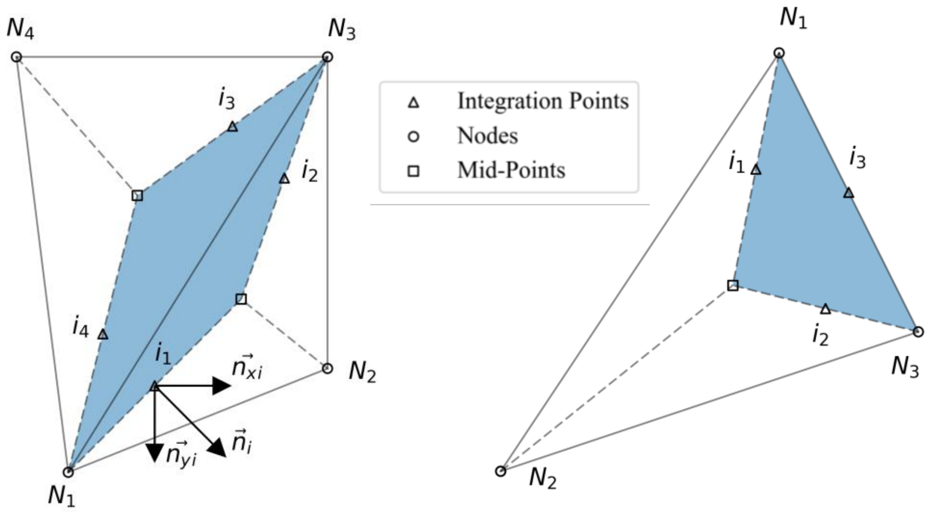

Fig. 2: Edge-Based Integration

With the integration points marked in Fig. 2, the integral of Eq. (11) can be represented as:

$$\hat{\boldsymbol{\varepsilon}}_C^m = \frac{1}{A_C} \sum_{i=1}^{M} \ell_i \begin{Bmatrix} n_{x_i} u_i \\ n_{y_i} v_i \\ n_{y_i} u_i + n_{x_i} v_i \end{Bmatrix}$$

$$\hat{\boldsymbol{\varepsilon}}_C^b = \frac{1}{A_C} \sum_{i=1}^{M} \ell_i \begin{Bmatrix} n_{x_i} \phi_{x_i} \\ n_{y_i} \phi_{y_i} \\ n_{y_i} \phi_{x_i} + n_{x_i} \phi_{y_i} \end{Bmatrix} \tag{12}$$

$$\begin{Bmatrix} \hat{w}_{,x_C} \\ \hat{w}_{,y_C} \end{Bmatrix} = \frac{1}{A_C} \sum_{i=1}^{M} \ell_i \begin{Bmatrix} n_{x_i} w_i \\ n_{y_i} w_i \end{Bmatrix}$$

where $M = 3$ for boundary edges and $M = 4$ for interior edges; ℓ_i is the length of the i^{th} straight segment where the i^{th} integration point lies. Quantities calculated at the i^{th} integration point are the normal vector components n_{x_i}, n_{y_i}; and the interpolated displacement field quantities u_i, v_i, w_i, ϕ_{x_i}, ϕ_{y_i}.

Letting $\boldsymbol{d}$ be a vector containing all of nodal degrees of freedom and $\boldsymbol{N^u}$, $\boldsymbol{N^v}$, $\boldsymbol{N^w}$, $\boldsymbol{N^{\phi_x}}$, $\boldsymbol{N^{\phi_y}}$ a set of interpolation functions, the displacement field can be approximated by:

$$\boldsymbol{u} = \begin{Bmatrix} u \\ v \\ w \\ \phi_x \\ \phi_y \end{Bmatrix} = \begin{bmatrix} \boldsymbol{N^u} \\ \boldsymbol{N^v} \\ \boldsymbol{N^w} \\ \boldsymbol{N^{\phi_x}} \\ \boldsymbol{N^{\phi_y}} \end{bmatrix} \boldsymbol{d} = \boldsymbol{N}\,\boldsymbol{d} \tag{13}$$

where $\boldsymbol{d}$ is defined as:

$$\boldsymbol{d^T} = \{u_1 \quad v_1 \quad w_1 \quad \phi_{x_1} \quad \phi_{y_1} \quad \cdots \quad u_N \quad v_N \quad w_N \quad \phi_{y_N} \quad \phi_{y_N}\} \tag{14}$$

Table 1 lists the interpolation weights for each integration point for both interior and boundary edges, noting that for boundary edges only 3 integration points are used. To illustrate the integration procedure, u_i calculated for a boundary edge at the integration point $i = 1$ would be $u_{i=1} = N_1^u d_1^u + N_2^u d_2^u + N_3^u d_3^u + N_4^u d_4^u$. Obtaining N_i from Table 1 $u_{i=1}$ becomes $u_{i=1} = \frac{2}{3} d_1^u + \frac{1}{6} d_2^u + \frac{1}{6} d_3^u + 0\, d_4^u$.

Table 1: Interpolation Points for Interior and Boundary Edges

		N_1	N_2	N_3	N_4
Interior	i_1	$\frac{2}{3}$	$\frac{1}{6}$	$\frac{1}{6}$	0
	i_2	$\frac{1}{6}$	$\frac{1}{6}$	$\frac{2}{3}$	0
	i_3	$\frac{1}{6}$	0	$\frac{2}{3}$	$\frac{1}{6}$
	i_4	$\frac{2}{3}$	0	$\frac{1}{6}$	$\frac{1}{6}$
Boundary	i_1	$\frac{2}{3}$	$\frac{1}{6}$	$\frac{1}{6}$	0
	i_2	$\frac{1}{6}$	$\frac{1}{6}$	$\frac{2}{3}$	0
	i_3	$\frac{1}{2}$	0	$\frac{1}{2}$	0

The numerical integration of Eq. (12) using the interpolation of Eq. (13) can be applied to Eq. (7) resulting in:

$$\delta \boldsymbol{d}^T (\boldsymbol{K_0} + \lambda\, \boldsymbol{K_G}) \delta \boldsymbol{d} = 0 \tag{15}$$

with:

$$\begin{gathered} \boldsymbol{K_0} = \boldsymbol{K_0^s} + \sum_{C=1}^{n} \boldsymbol{K_{0C}} \\ \boldsymbol{K_G} = \sum_{C=1}^{n} \boldsymbol{K_{GC}} \\ \boldsymbol{K_{0C}} = A_C \left[\hat{\varepsilon}_{iC}^{m} A_{ij_C} \hat{\varepsilon}_{jC}^{m} + \hat{\varepsilon}_{iC}^{m} B_{ij_C} \hat{\varepsilon}_{jC}^{b} + \hat{\varepsilon}_{iC}^{b} B_{ij_C} \hat{\varepsilon}_{jC}^{m} + \hat{\varepsilon}_{iC}^{b} D_{ij_C} \hat{\varepsilon}_{jC}^{b} \right] \\ \boldsymbol{K_{GC}} = A_C\, \widehat{w},_{iC}\, N_{ij_C}\, \widehat{w},_{jC} \end{gathered} \tag{16}$$

where $\boldsymbol{K_0}$ is the constitutive stiffness matrix, $\boldsymbol{K_0^s}$ contains the stiffnesses due to the transverse shear strain terms ε_{iC}^{s} and will be covered in the next section, cf. Eq. (25); $\boldsymbol{K_G}$ is the geometric stiffness matrix, or initial stress stiffness matrix [37], taking into account the stiffness change due to an initial membrane stress state N_{ij_C}. The initial membrane stress state N_{ij_C} is computed directly from the constant smoothed strain quantities using Eq. (17), where $\hat{\varepsilon}_{jC}^{m}$ and $\hat{\varepsilon}_{jC}^{b}$ are computed based on static results. The suggested procedure to smooth the constitutive properties in order to obtain A_{ij_C}, B_{ij_C} and D_{ij_C} for each subdomain Ω_C is detailed in Section 3.

$$N_{ij_C} = A_{ij_C}\hat{\varepsilon}^{m}_{jc} + B_{ij_C}\hat{\varepsilon}^{b}_{jc} \tag{17}$$

Note in Eq. (15) that a load multiplier λ is used to transform the equation in an eigenvalue problem. Assuming any arbitrary quantity for the first variation $\delta\boldsymbol{d}$ [43], say $\delta\boldsymbol{d} = \boldsymbol{d_1}$, Eq. (15) becomes:

$$\delta\boldsymbol{d}(\boldsymbol{K_0} + \lambda\,\boldsymbol{K_G})\boldsymbol{d_1} = 0 \tag{18}$$

which must hold true for any variation $\delta\mathbf{d}$. Therefore, the following eigenvalue problem is obtained:

$$(\boldsymbol{K_0} + \lambda\,\boldsymbol{K_G})\boldsymbol{d_1} = \{0\} \tag{19}$$

which can be rearranged to:

$$\left(\boldsymbol{K_G} + \frac{1}{\lambda}\,\boldsymbol{K_0}\right)\boldsymbol{d_1} = \{0\} \tag{20}$$

in order to be numerically solved in a more robust and efficient way, as proposed by Castro [44]. Eq. (20) takes advantage of the higher sparsity of matrix $\boldsymbol{K_G}$ compared to $\boldsymbol{K_0}$, where for each computed eigenvalue $1/\lambda$, there is a corresponding eigenvector $\boldsymbol{d_1}$.

2.1 Transverse Shear Strain Smoothing

In the previous section the contribution of the transverse shear strains to the constitutive matrices derived using strain smoothing was not considered. The present section demonstrates how the Discrete Shear Gap (DSG) method, developed by Bletzinger et al. [32] is adopted, producing a numerical solution free of shear locking [2,32,33].

The transverse shear strain vector for each integration sub-domain Ω_s, $\boldsymbol{\varepsilon}^{s}_{\boldsymbol{\Omega}}$, is defined using Eq. (21), for $\sum\Omega_s = \Omega$ and $\Omega_i \cap \Omega_j = 0$. Note that Ω_s is not necessarily equal to Ω_C previously used for strain smoothing. In fact, for all DSG methods herein presented, Ω_s represents a single triangle of the background mesh.

$$\boldsymbol{\varepsilon}^{s}_{\boldsymbol{\Omega_s}} = \begin{Bmatrix}\gamma_{xz}\\ \gamma_{yz}\end{Bmatrix} = \boldsymbol{B}^{s}_{\boldsymbol{\Omega_s}}\,\boldsymbol{d_{\Omega_s}} \tag{21}$$

where

$$\boldsymbol{B}^{s}_{\boldsymbol{\Omega_s}} = \frac{1}{2A_\Delta}\left[\begin{array}{ccc|ccc|ccc} b_\Delta - d_\Delta & A_\Delta & 0 & d_\Delta & \frac{a_\Delta d_\Delta}{2} & \frac{b_\Delta d_\Delta}{2} & -b_\Delta & -\frac{b_\Delta c_\Delta}{2} & -\frac{b_\Delta d_\Delta}{2} \\ c_\Delta - a_\Delta & 0 & A_\Delta & -c_\Delta & -\frac{a_\Delta c_\Delta}{2} & -\frac{b_\Delta c_\Delta}{2} & a_\Delta & \frac{a_\Delta c_\Delta}{2} & \frac{a_\Delta d_\Delta}{2} \end{array}\right] \tag{22}$$

and

$$\boldsymbol{d}^{\boldsymbol{T}}_{\boldsymbol{\Omega_s}} = \{w_1 \quad \phi_{x_1} \quad \phi_{y_1} | w_2 \quad \phi_{x_2} \quad \phi_{y_2} | w_3 \quad \phi_{x_3} \quad \phi_{y_3}\} \tag{23}$$

Parameters a_Δ, b_Δ, c_Δ, d_Δ are explicitly calculated from the nodal coordinates as illustrated in Fig. 3 and defined in Eq. (24); A_Δ is the area of the triangle; w_i, ϕ_{x_i} and ϕ_{y_i} are respectively the normal displacement and the two shell rotations for the i^{th} node. Note that in the DSG the actual nodal coordinates are directly used, with no need to make use of Jacobians.

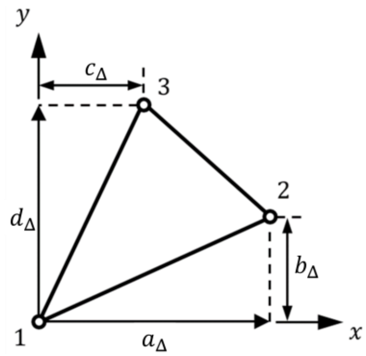

Fig. 3: Three node domain, modified from Bletzinger et al. [32]

$$\begin{aligned} a_\Delta &= x_2 - x_1 \\ b_\Delta &= y_2 - y_1 \\ c_\Delta &= x_3 - x_1 \\ d_\Delta &= y_3 - y_1 \end{aligned} \tag{24}$$

In Eq. (21) $\mathbf{B}_{\Omega_s}^{s}$ is a constant matrix that can directly be used to calculate $\boldsymbol{K}_0^s$ of Eq. (16) as:

$$\begin{gathered}\boldsymbol{K}_0^s = \sum \boldsymbol{K}_{0_{\Omega_s}}^s \\ \boldsymbol{K}_{0_{\Omega_s}}^s = \boldsymbol{B}_{\Omega_s}^{s\ T}\, \widehat{\boldsymbol{E}}_{\Omega_s}\, \boldsymbol{B}_{\Omega_s}^s\end{gathered} \tag{25}$$

where $\widehat{\boldsymbol{E}}_{\boldsymbol{\Omega}_s}$ differs from the transverse shear terms E_{ij} defined in Eq. (5) because when the DSG is used, E_{ij} must be stabilized. Lyly et al. [34] proposed a stabilization method, also called Stenberg`s method [45], where the terms of $\widehat{\boldsymbol{E}}_{\boldsymbol{\Omega}_s}$ are defined as:

$$\hat{E}_{\Omega_{s}ij} = \frac{\kappa}{1+\dfrac{\alpha \ell_{\Omega_s}^2}{h_{\Omega_s}^2}} \begin{bmatrix} \bar{Q}_{13_{\Omega_s}} & 0 \\ 0 & \bar{Q}_{23_{\Omega_s}} \end{bmatrix} \tag{26}$$

where h_{Ω_s} is the plate thickness adopted for Ω_s, ℓ_{Ω_s} is the longest edge of the corresponding triangle used in the DSG computation (or sub-triangle, as discussed in the subsequent paragraphs); α is a positive constant parameter, which was investigated by Lyly et al. [34] using linear static analyses and is investigated in the present study for linear buckling analysis, cf. Section 5; κ is the shear correction factor, herein calculated according to Vlachoutsis [46]. Despite shear correction factors are still applied, the conclusion of Lyly et al. [34] is that κ is no longer a very relevant parameter when the stabilization scheme of Eq. (26) is used, since other parameters based on the geometry of the integrated domain and even the parameter α will have a greater influence than κ. The quantities $\overline{\mathrm{Q}}_{13_{\Omega_s}}$ and $\overline{\mathrm{Q}}_{23_{\Omega_s}}$ are averaged laminate transverse shear stiffnesses. At each i^{th} node quantities $\overline{\mathrm{Q}}_{13_{\mathrm{i}}}$ and $\overline{\mathrm{Q}}_{23_i}$ are computed using Eq. (27), subsequently averaged using Eq. (35) to obtain $\overline{\mathrm{Q}}_{13_{\Omega_s}}$ and $\overline{\mathrm{Q}}_{23_{\Omega_s}}$. The transverse shear stiffnesses G_{13_k} and G_{23_k} are material properties of the k^{th} lamina. The plate thickness h_{Ω_s} is also averaged using Eq. (35), after having the plate thickness computed at each i^{th} node.

$$\begin{gathered}\bar{Q}_{13_i} = \sum\nolimits_k \left(z_{sup_k} - z_{inf_k}\right) G_{13_k} \\ \bar{Q}_{23_i} = \sum\nolimits_k \left(z_{sup_k} - z_{inf_k}\right) G_{23_k}\end{gathered} \tag{27}$$

Despite the superior properties of the DSG method, Nguyen-Thoi et al. [8] have shown through numerical analyses that the DSG method possesses over-stiffened properties. For overcoming this over-stiffened behaviour, a cell-based smoothing approach proposed by Phung-Van et al. [33] is herein adopted. Fig. 4 illustrates how this approach is carried out. Nodes 1, 2 and 3 delimit a mesh triangle that is subdivided in three sub-triangles Δ_1, Δ_2 and Δ_3, which are then used in the DSG. Parameters a_Δ, b_Δ, c_Δ, d_Δ can be defined for each sub-triangle using Eq. (28).

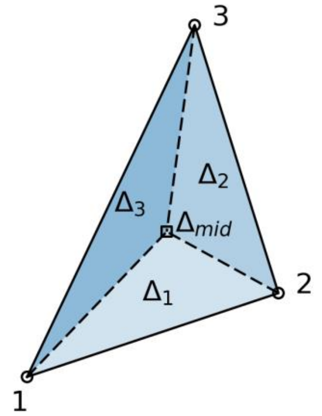

Fig. 4: Cell-based smoothing for transverse shear strains

$$\begin{array}{lll} a_{\Delta_1} = x_1 - x_{mid} & a_{\Delta_2} = x_2 - x_{mid} & a_{\Delta_3} = x_3 - x_{mid} \\ b_{\Delta_1} = y_1 - y_{mid} & b_{\Delta_2} = y_2 - y_{mid} & b_{\Delta_3} = y_3 - y_{mid} \\ c_{\Delta_1} = x_2 - x_{mid} & c_{\Delta_2} = x_3 - x_{mid} & c_{\Delta_3} = x_1 - x_{mid} \\ d_{\Delta_1} = y_2 - y_{mid} & d_{\Delta_2} = y_3 - y_{mid} & d_{\Delta_3} = y_1 - y_{mid} \end{array} \tag{28}$$

with

$$x_{mid} = (x_1 + x_2 + x_3)/3$$
$$y_{mid} = (y_1 + y_2 + y_3)/3 \tag{29}$$

The corner sequence for each sub-triangle is important for the DSG, with the following sequence being herein adopted: $\Delta_1: \Delta_{mid} \rightarrow 1 \rightarrow 2$; $\Delta_2: \Delta_{mid} \rightarrow 2 \rightarrow 3$; $\Delta_3: \Delta_{mid} \rightarrow 3 \rightarrow 1$. The following auxiliary matrices are computed for the first sub-triangle $\Delta_1: \Delta_{mid} \rightarrow 1 \rightarrow 2$.

$$\Delta_{1_{mid}} = \begin{bmatrix} b_{\Delta 1} - d_{\Delta 1} & A_{\Delta 1} & 0 \\ c_{\Delta 1} - a_{\Delta 1} & 0 & A_{\Delta 1} \end{bmatrix}$$
$$\Delta_{1_{N1}} = \begin{bmatrix} d_{\Delta 1} & a_{\Delta_1} d_{\Delta_1}/2 & b_{\Delta_1} d_{\Delta_1}/2 \\ -c_{\Delta 1} & -a_{\Delta_1} c_{\Delta_1}/2 & -b_{\Delta_1} c_{\Delta_1}/2 \end{bmatrix} \tag{30}$$
$$\Delta_{1_{N2}} = \begin{bmatrix} -b_{\Delta 1} & -b_{\Delta_1} c_{\Delta_1}/2 & -b_{\Delta_1} d_{\Delta_1}/2 \\ a_{\Delta 1} & a_{\Delta_1} c_{\Delta_1}/2 & a_{\Delta_1} d_{\Delta_1}/2 \end{bmatrix}$$

Similarly, for the second sub-triangle $\Delta_2: \Delta_{mid} \rightarrow 2 \rightarrow 3$:

$$\Delta_{2_{mid}} = \begin{bmatrix} b_{\Delta 2} - d_{\Delta 2} & A_{\Delta 2} & 0 \\ c_{\Delta 2} - a_{\Delta 2} & 0 & A_{\Delta 2} \end{bmatrix}$$
$$\Delta_{2_{N2}} = \begin{bmatrix} d_{\Delta 2} & a_{\Delta_2} d_{\Delta_2}/2 & b_{\Delta_2} d_{\Delta_2}/2 \\ -c_{\Delta 2} & -a_{\Delta_2} c_{\Delta_2}/2 & -b_{\Delta_2} c_{\Delta_2}/2 \end{bmatrix} \tag{31}$$
$$\Delta_{2_{N3}} = \begin{bmatrix} -b_{\Delta 2} & -b_{\Delta_2} c_{\Delta_2}/2 & -b_{\Delta_2} d_{\Delta_2}/2 \\ a_{\Delta 2} & a_{\Delta_2} c_{\Delta_2}/2 & a_{\Delta_2} d_{\Delta_2}/2 \end{bmatrix}$$

For the third sub-triangle $\Delta_3: \Delta_{mid} \rightarrow 3 \rightarrow 1$:

$$\Delta_{3_{mid}} = \begin{bmatrix} b_{\Delta 3} - d_{\Delta 3} & A_{\Delta 3} & 0 \\ c_{\Delta 3} - a_{\Delta 3} & 0 & A_{\Delta 3} \end{bmatrix}$$
$$\Delta_{3_{N3}} = \begin{bmatrix} d_{\Delta 3} & a_{\Delta_3} d_{\Delta_3}/2 & b_{\Delta_3} d_{\Delta_3}/2 \\ -c_{\Delta 3} & -a_{\Delta_3} c_{\Delta_3}/2 & -b_{\Delta_3} c_{\Delta_3}/2 \end{bmatrix} \tag{32}$$
$$\Delta_{3_{N1}} = \begin{bmatrix} -b_{\Delta 3} & -b_{\Delta_3} c_{\Delta_3}/2 & -b_{\Delta_3} d_{\Delta_3}/2 \\ a_{\Delta 3} & a_{\Delta_3} c_{\Delta_3}/2 & a_{\Delta_3} d_{\Delta_3}/2 \end{bmatrix}$$

Using the auxiliary matrices of Eqs. (30) – (32), the transverse shear matrices for each sub-triangle can be built as:

$$\boldsymbol{B}^s_{\Delta_1} = \frac{1}{2A_{\Delta_1}} \left[\frac{1}{3}\Delta_{1_{mid}} + \Delta_{1_{N1}} \;\middle|\; \frac{1}{3}\Delta_{1_{mid}} + \Delta_{1_{N2}} \;\middle|\; \frac{1}{3}\Delta_{1_{mid}} \right]$$
$$\boldsymbol{B}^s_{\Delta_2} = \frac{1}{2A_{\Delta_2}} \left[\frac{1}{3}\Delta_{2_{mid}} \;\middle|\; \frac{1}{3}\Delta_{2_{mid}} + \Delta_{2_{N2}} \;\middle|\; \frac{1}{3}\Delta_{2_{mid}} + \Delta_{2_{N3}} \right] \tag{33}$$
$$\boldsymbol{B}^s_{\Delta_3} = \frac{1}{2A_{\Delta_3}} \left[\frac{1}{3}\Delta_{3_{mid}} + \Delta_{3_{N1}} \;\middle|\; \frac{1}{3}\Delta_{3_{mid}} \;\middle|\; \frac{1}{3}\Delta_{3_{mid}} + \Delta_{3_{N3}} \right]$$

Finally, matrix $\boldsymbol{B}^s_{\boldsymbol{\Omega_s}}$ for the smoothed integration cell is calculated using the weighted average of Eq. (34).

$$\boldsymbol{B}^s_{\boldsymbol{\Omega_s}} = \frac{1}{A_\Delta}\left(A_{\Delta_1} \boldsymbol{B}^s_{\boldsymbol{\Delta_1}} + A_{\Delta_2} \boldsymbol{B}^s_{\boldsymbol{\Delta_2}} + A_{\Delta_3} \boldsymbol{B}^s_{\boldsymbol{\Delta_3}} \right) \tag{34}$$

3. Heterogeneity of Constitutive Properties

Modern manufacturing techniques of variable stiffness laminated composite materials, such as automatic fiber placement or continuous tow shearing [47], allow the use of variable fiber directions along the laminated shell structure, significantly increasing the tailoring potential of novel designs.

In the present study constitutive properties A_{ij}, B_{ij}, D_{ij}, E_{ij} that should be integrated over Ω_C as per Eq. (7) must assume a constant smoothed value within Ω_C due to the strain smoothing, where the integration is performed using Eq. (16). The proposed smoothing approach starts with the constitutive properties calculated at each node, followed by a linear interpolation of the constitutive properties in Ω_C assuming that the properties of each subdomain should be those at the centroid of Ω_C, as illustrated in Fig. 5. For each integration cell belonging to an interior edge there are four nodes involved, whereas for boundary edges only three nodes are involved, such that Eq. (35) may be used to compute the smoothed properties at the centroid of Ω_C, where A_{ij_k} are the properties at the k^{th} node. For B_{ij_C}, D_{ij_C} and E_{ij_C} the approach is analogous. The interpolation weights f_k of Eq. (35) are given in Table 2.

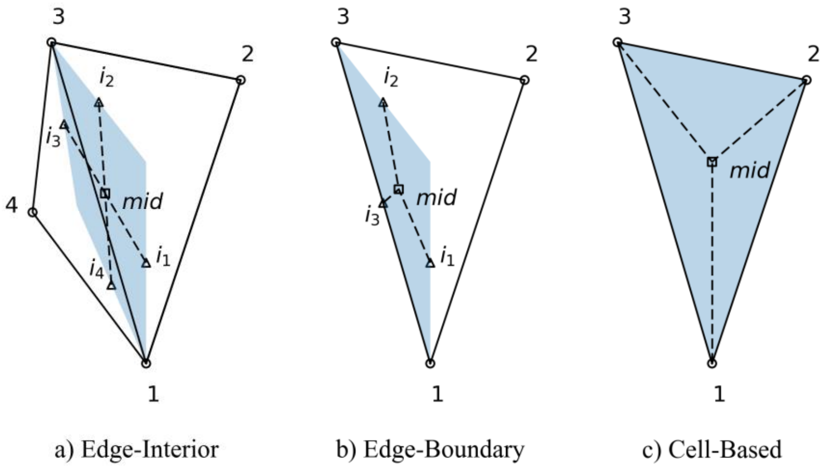

Fig. 5: Interpolation scheme for constitutive properties

$$A_{ij_C} = f_1 A_{ij_1} + f_2 A_{ij_2} + f_3 A_{ij_3} + f_4 A_{ij_4} \tag{35}$$

Table 2: Interpolation weights f_k for constitutive matrices

	f_1	f_2	f_3	f_4
Edge-based Interior	$\frac{5}{12}$	$\frac{1}{12}$	$\frac{5}{12}$	$\frac{1}{12}$
Edge-based Boundary	$\frac{4}{9}$	$\frac{1}{9}$	$\frac{4}{9}$	0
Cell-based	$\frac{1}{3}$	$\frac{1}{3}$	$\frac{1}{3}$	0

4. Variable Ply Thickness

The proposed laminate is composed of layers formed by the successive deposition of tows with varying angle φ, as illustrated in Fig. 6. The shifting direction is followed by the tape laying machine head after finishing the deposition one tow [48].

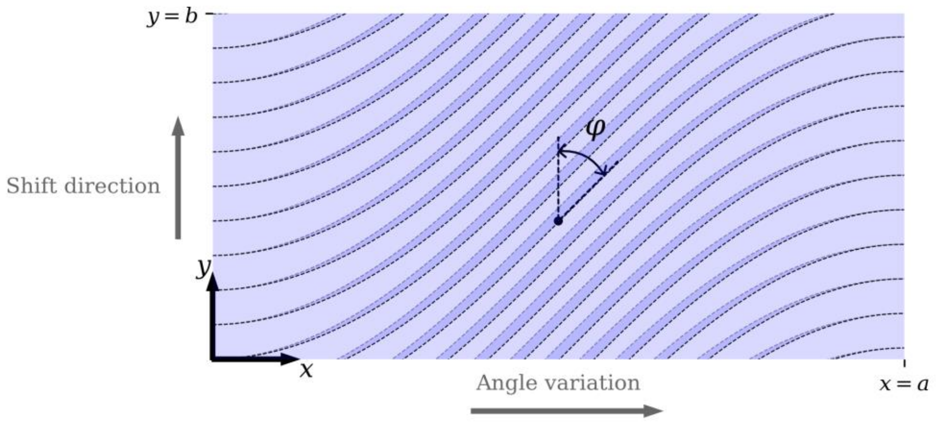

Fig. 6: Ply with variable thickness formed after the deposition of successive tows

The dashed lines in Fig. 6 are each tow's edging lines, whereas the darker regions represent ply overlaps, characteristic of tow-steered layers laid up by automated fiber placement (AFP). The minimum amount of tow overlap within a deposited ply is achieved when the deposition shift is the same as the minimum effective tow width $\min(w_e(x,y))$, as demonstrated by Blom et al. [48]. Shift values smaller than the minimum w_e would produce additional and unnecessary overlapping, whereas higher values would render ply gaps. Fig. 7 illustrates the dependency between the effective tow width w_e and the tow width w_{tow}. Eq. (36) is an approximated formula for w_e proposed by Blom et al. [48].

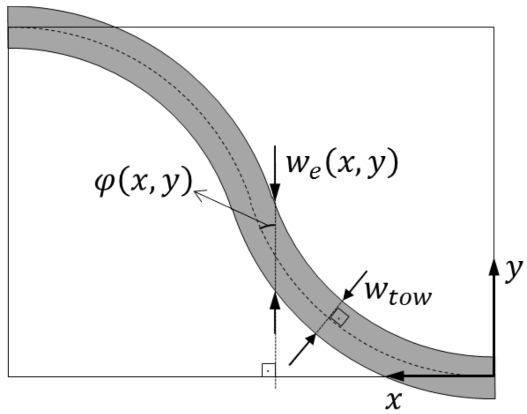

Fig. 7: Variable angle tow

$$w_e(x,y) \approx \frac{w_{tow}}{sin\big(\varphi(x,y)\big)} \tag{36}$$

In the present study $\varphi(x,y) = \varphi(x),\ \forall y$; being $\varphi(x)$ calculated using 3 control points in the Lagrange interpolation scheme proposed by Wu et al. [49]. According to Eq. (36), the values of φ of [45º, 30º, 20º] result in w_e of approximately [1.4, 2.0, 2.9]× w_{tow}, producing the layers illustrated in Fig. 8.

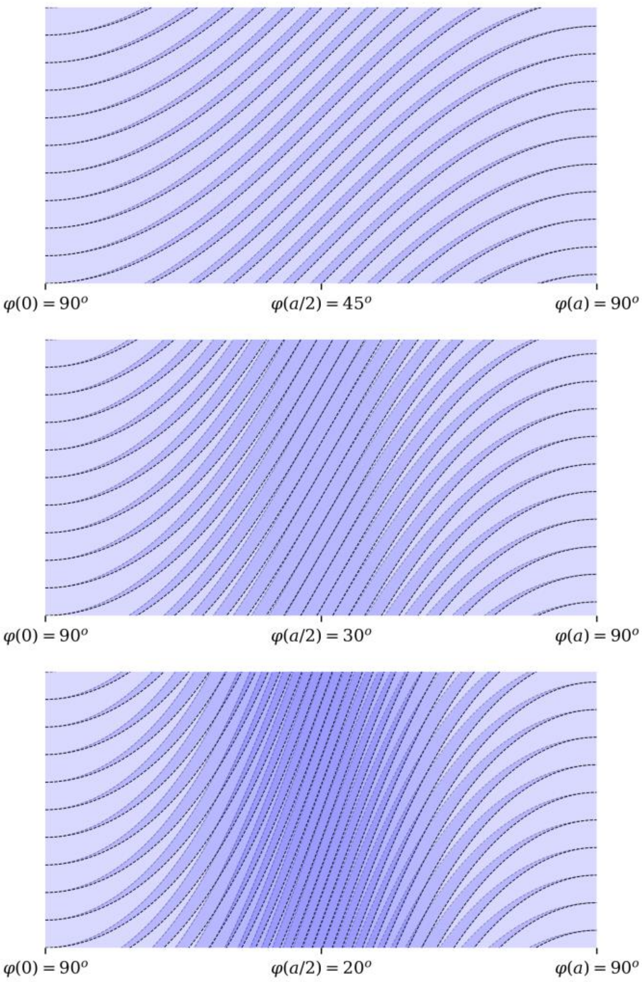

Fig. 8: Tow steered layers for different φ values

In order to simplify the structural modelling of complex thickness distributions such as the ones shown in Fig. 8, a smeared thickness approach is proposed. Fig. 9 illustrates two cross sections of the first tow steered layer with $\varphi(a/2) = 45^o$ of Fig. 8.

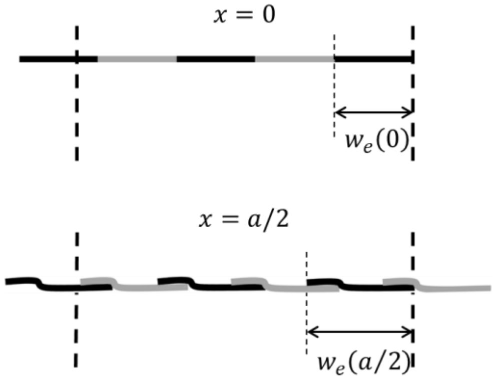

Fig. 9: Cross section view of tows

For any arbitrarily fixed width along y the same amount of tows will be placed due to the fixed shift of the tow steering machine. Considering that along the width b there are n_{tows} tows results in $b = n_{tows} \times w_{tow}$. The cross-section area at any x position is $A = n_{tows} \times h_{tow} \times w_e$. Defining a smeared thickness h_e the smeared cross section area becomes $A_e = h_e \times b = h_e \times n_{tows} \times w_{tow}$. Making $A = A_e$ guarantees that h_e results in the same material volume as the real thickness distribution, resulting in Eq. (37).

$$h_e(x) = h_{tow} \frac{w_e(x)}{w_{tow}} \approx \frac{h_{tow}}{sin(\varphi(x))} \tag{37}$$

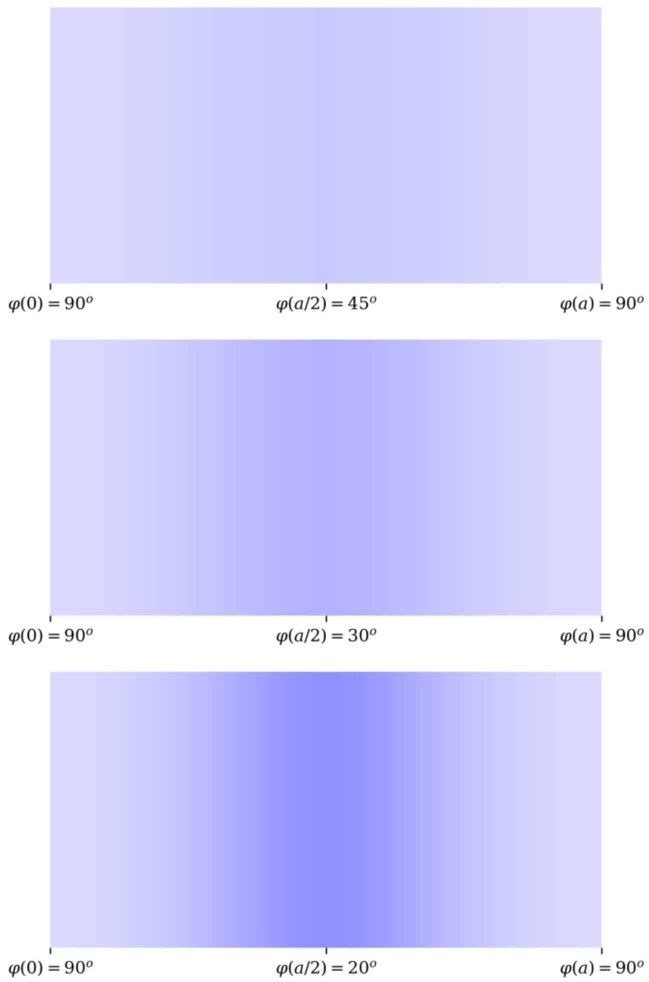

Fig. 10: Smeared thickness distribution for different φ values

Newer manufacturing techniques such as the continuous tow shearing (CTS) [47] would not produce the overlaps observed in Fig. 8. Applying the CTS, Groh and Weaver [50] arrived at a similar equation than Eq. (37), but in their study the numerical thickness averaging of Eq. (37) (cf. Fig. 10) is no longer an approximation since the CTS already produces tows with varying thickness in order to keep a constant volume.

5. Verifications against conventional FEM

Convergence studies evaluating the first linear buckling eigenvalue are performed in three types of laminates: quasi-isotropic $[0, 90, +45, -45]_{sym}$, anisotropic asymmetric $[-30, -30, 0., 0, -45, -45]$ and variable stiffness. The variable stiffness laminate consists of two plies, with each ply having its tows steered using $w_{tow} = 0.1m$, varying the angle using a second order Lagrange polynomial with 3 control points at $x = [0, a/2, a]$, with respective control angles of $[0, +45, 0]$ for the first ply and $[0, -45, 0]$ for the second ply, producing the pattern shown in Fig. 11. A uniformly distributed unitary compressive load $\widehat{N}_{xx} = 1\ N/m$ is applied in order to compute the static distribution of membrane stresses N_{ij_C} used to compute $\boldsymbol{K_{GC}}$ in Eq. (16). The following orthotropic material properties and fixed geometric parameters were adopted along all studies: $E_{11} = 129\ GPa$, $E_{22} = 9.37\ GPa$, $\nu_{12} = 0.38$, $G_{12} = G_{13} = G_{23} = 5.24\ GPa$, $h_{ply} = 1.9\ 10^{-4}m$, $b = 1m$.

Note that some laminate configurations are asymmetric, with $B_{ij} \neq 0$, meaning that they will bend under any in-plane loads. This bending already causes normal displacements following a single load-displacement path, therefore not undergoing bifurcation at the critical compressive load [51]. The apparent inconsistency in presenting linear buckling results for asymmetric laminates has the purpose of evaluating the ES-PIM for more general laminates.

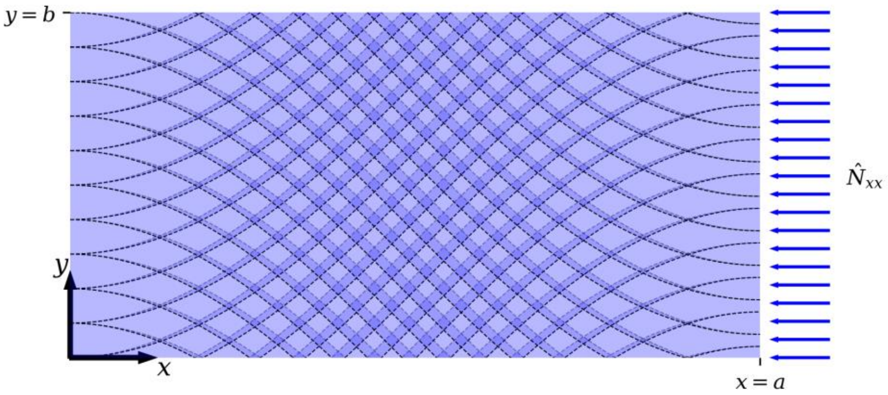

Fig. 11: Variable stiffness laminate with 2 plies

The number of elements along x was varied from 2 to 40, with two refinement levels illustrated in Fig. 12 for $a/b = 0.5$. Results for $a/b = 0.5$ and $a/b = 3.0$ are herein presented, and the authors verified that a/b ratios of 1.0 and 2.0 showed the same convergence behavior. FEM analysis were performed using NX Nastran Version 10.2, in a Windows 10 64-bit operational system, adopting always the same triangular mesh used for ES-PIM. Parameters such as K6ROT and transverse shear stiffness in Nastran were changed by the authors during this convergence study, showing very little effect for all linear buckling analyses. When heterogeneous properties exist over the domain, in the FEM analyses one laminate property is assigned for each element, whereas in the ES-PIM the methodology explained in Section 3 is used. The geometric boundary conditions consist on $u = v = w = 0$ at $x = 0$; $v = w = 0$ at $y = 0$ and $y = b$; and $w = 0$ at $x = a$.

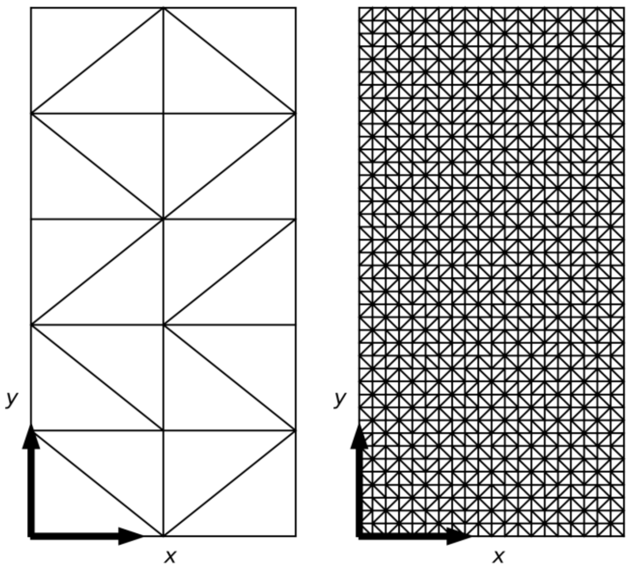

Fig. 12: Mesh with 2 and 20 elements along x, for $a/b = 0.5$

An investigation on the effect of parameter α used in the corrected transverse shear stiffness of the DSG is carried out by varying α from 0.05 to 0.15. It is important to mention that the value of $\alpha = 0.10$ was adopted by Bischoff and Bletzinger [45] and Lyly et al. [34]. In the present study the authors decided to carry out this investigation on α because $\alpha = 0.10$ was resulting in a too flexible linear buckling behavior for some cases, as discussed next.

The convergence results for $a/b = 0.5$ are shown in Table 3 – Table 5, while the results for $a/b = 3.0$ are shown in Table 6 – Table 8. It can be seen that for all cases Nastran and the ES-PIM converged to the same result. Fig. 13 illustrates a normalized 1^{st} eigenvalue defined as $\lambda^* = \lambda/\lambda_{converged} - 1$ for the values of Table 3 – Table 8. The blue horizontal line at $\lambda^* = 0$ represents the converged value. It becomes convenient to visualize how α affects the ES-PIM convergence behavior. For $\alpha = 0.1$ the curves are highlighted, where the overly flexible linear buckling behavior can be easily noticed for the quasi-isotropic and anisotropic laminates when $a/b = 0.5$, converging from a softer solution. Using $\alpha = 0.15$ led to a convergence from below also for $a/b = 3.0$ for these two laminates. For the variable stiffness laminate the observed convergence was always from a stiffer solution. Regarding convergence rates, the ES-PIM demonstrated to be superior than Nastran`s CTRIA3, specially for α between 0.07 and 0.09. For $\alpha < 0.07$ the convergence rate is comparable to CTRIA3, whereas for $\alpha > 0.09$ convergence from below was observed.

From the design point of view the use of higher α values ($\alpha > 0.09$) will result in conservative estimates of the critical buckling load, which can be advantageous when one is uncertain about the convergence characteristic of a given mesh. However, if a precise estimate of the buckling load is preferred, based on the current numerical studies the authors suggest keeping α within 0.07 and 0.09. It is known in the literature that a method similar to the ES-PIM called node-based smoothed point interpolation method (NS-PIM) shows convergence from below for vibration problems [2], but the fact that the ES-PIM also showed a convergence from a softer solution has proved to be a remarkable characteristic of the method that should be further explored in future studies.

Table 3 – Critical buckling load [N], quasi-isotropic, $a/b = 0.5$

Elements along x	ES-PIM $\alpha = 0.05$	ES-PIM $\alpha = 0.06$	ES-PIM $\alpha = 0.07$	ES-PIM $\alpha = 0.08$	ES-PIM $\alpha = 0.09$	ES-PIM $\alpha = 0.10$	ES-PIM $\alpha = 0.15$	FEM
2	1298.45	1211.90	1136.82	1070.97	1012.67	960.64	766.12	1315.09
3	1149.67	1112.07	1077.13	1044.51	1013.94	985.21	863.78	1179.12
4	1155.28	1120.62	1088.25	1057.87	1029.28	1002.28	886.87	1172.52
5	1080.70	1066.58	1052.92	1039.67	1026.80	1014.28	956.33	1102.86
6	1073.91	1063.83	1054.00	1044.40	1035.01	1025.82	982.48	1089.54
7	1068.77	1061.16	1053.72	1046.42	1039.25	1032.20	998.59	1081.03
8	1065.31	1059.39	1053.57	1047.85	1042.21	1036.66	1009.93	1076.19
9	1066.18	1060.53	1054.97	1049.50	1044.12	1038.81	1013.23	1076.09
10	1063.74	1059.17	1054.68	1050.24	1045.87	1041.55	1020.64	1072.17
15	1059.97	1058.09	1056.24	1054.40	1052.57	1050.77	1041.91	1063.86
20	1059.33	1058.21	1057.09	1055.99	1054.90	1053.82	1048.50	1061.79
30	1059.03	1058.47	1057.93	1057.38	1056.84	1056.31	1053.69	1060.32
40	1059.00	1058.65	1058.30	1057.96	1057.62	1057.28	1055.62	1059.81

Table 4 – Critical buckling load [N], anisotropic, $a/b = 0.5$

Elements along x	ES-PIM $\alpha = 0.05$	ES-PIM $\alpha = 0.06$	ES-PIM $\alpha = 0.07$	ES-PIM $\alpha = 0.08$	ES-PIM $\alpha = 0.09$	ES-PIM $\alpha = 0.10$	ES-PIM $\alpha = 0.15$	FEM
2	471.50	440.29	413.28	389.63	368.73	351.10	280.60	590.28
3	411.77	397.21	383.97	371.81	360.55	350.09	306.67	468.39
4	414.14	401.31	389.50	378.55	368.31	358.70	317.96	459.02
5	382.79	377.30	372.08	367.08	362.29	357.66	336.64	407.33
6	376.85	372.97	369.26	365.67	362.20	358.83	343.18	391.83
7	374.36	371.35	368.46	365.66	362.95	360.31	347.96	385.71
8	372.47	370.07	367.76	365.53	363.36	361.25	351.32	383.78
9	373.07	370.78	368.57	366.44	364.36	362.34	352.80	382.57
10	371.52	369.65	367.86	366.11	364.41	362.75	354.88	380.22
15	369.25	368.34	367.48	366.64	365.83	365.03	361.31	374.41
20	368.08	367.52	366.98	366.45	365.95	365.45	363.10	370.68
30	367.99	367.64	367.31	367.00	366.70	366.41	365.06	370.26
40	367.61	367.39	367.17	366.96	366.76	366.57	365.65	368.87

Table 5 – Critical buckling load [N], variable stiffness, $a/b = 0.5$

Elements along x	ES-PIM $\alpha = 0.05$	ES-PIM $\alpha = 0.06$	ES-PIM $\alpha = 0.07$	ES-PIM $\alpha = 0.08$	ES-PIM $\alpha = 0.09$	ES-PIM $\alpha = 0.10$	ES-PIM $\alpha = 0.15$	FEM
2	28.35	26.74	25.31	24.05	22.91	21.88	17.91	21.96
3	18.70	18.22	17.78	17.36	16.96	16.59	14.98	18.10
4	18.61	18.18	17.77	17.39	17.03	16.69	15.20	17.88
5	15.71	15.55	15.39	15.24	15.10	14.96	14.30	15.60
6	15.30	15.19	15.08	14.97	14.87	14.77	14.29	15.22
7	15.03	14.95	14.86	14.78	14.70	14.63	14.26	14.96
8	14.84	14.78	14.71	14.65	14.59	14.53	14.24	14.85
9	14.85	14.79	14.73	14.67	14.61	14.55	14.27	14.85
10	14.72	14.67	14.62	14.57	14.52	14.48	14.25	14.73
15	14.43	14.41	14.39	14.37	14.35	14.33	14.24	14.46
20	14.37	14.35	14.34	14.33	14.32	14.30	14.25	14.39
30	14.32	14.31	14.31	14.30	14.29	14.29	14.26	14.34
40	14.30	14.30	14.30	14.29	14.29	14.28	14.26	14.32

Table 6 – Critical buckling load [N], quasi-isotropic, $a/b = 3.0$

Elements along x	ES-PIM $\alpha = 0.05$	ES-PIM $\alpha = 0.06$	ES-PIM $\alpha = 0.07$	ES-PIM $\alpha = 0.08$	ES-PIM $\alpha = 0.09$	ES-PIM $\alpha = 0.10$	ES-PIM $\alpha = 0.15$	FEM
2	436.84	413.84	393.45	375.15	358.58	343.49	284.04	402.10
3	378.23	369.01	360.39	352.28	344.59	337.28	305.32	367.66
4	375.48	367.14	359.33	351.95	344.94	338.26	308.79	362.97
5	347.44	344.00	340.69	337.49	334.38	331.35	317.23	345.82
6	341.72	339.25	336.86	334.54	332.28	330.07	319.64	342.34
7	339.13	337.25	335.42	333.65	331.90	330.20	322.07	339.76
8	337.71	336.22	334.76	333.34	331.95	330.58	324.04	338.03
9	337.63	336.20	334.82	333.47	332.15	330.86	324.65	337.67
10	336.36	335.21	334.08	332.98	331.90	330.83	325.71	336.81
15	333.84	333.32	332.81	332.31	331.82	331.34	329.00	334.33
20	333.29	332.96	332.64	332.32	332.01	331.71	330.23	333.67
30	332.96	332.78	332.61	332.44	332.27	332.11	331.32	333.23
40	332.89	332.77	332.65	332.54	332.43	332.32	331.79	333.09

Table 7 – Critical buckling load [N], anisotropic, $a/b = 3.0$

Elements along x	ES-PIM $\alpha = 0.05$	ES-PIM $\alpha = 0.06$	ES-PIM $\alpha = 0.07$	ES-PIM $\alpha = 0.08$	ES-PIM $\alpha = 0.09$	ES-PIM $\alpha = 0.10$	ES-PIM $\alpha = 0.15$	FEM
2	211.27	199.06	188.40	178.72	169.66	161.19	128.52	186.99
3	171.61	166.26	161.47	157.10	153.05	149.26	132.99	173.94
4	174.02	169.04	164.50	160.29	156.34	152.60	136.27	171.39
5	161.03	158.61	156.38	154.28	152.29	150.38	141.70	165.25
6	157.50	155.76	154.15	152.62	151.15	149.74	143.27	158.31
7	154.48	153.15	151.89	150.70	149.55	148.44	143.32	156.33
8	153.72	152.59	151.54	150.53	149.57	148.65	144.40	156.80
9	153.49	152.43	151.43	150.49	149.58	148.71	144.67	155.09
10	152.70	151.80	150.96	150.16	149.40	148.66	145.24	154.26
15	151.44	150.93	150.46	150.01	149.59	149.18	147.32	153.54
20	150.95	150.59	150.26	149.94	149.65	149.36	148.06	152.51
30	150.77	150.56	150.35	150.16	149.97	149.80	148.99	151.98
40	150.71	150.55	150.40	150.26	150.12	149.99	149.40	151.57

Table 8 – Critical buckling load [N], variable stiffness, $a/b = 3.0$

Elements along x	ES-PIM $\alpha = 0.05$	ES-PIM $\alpha = 0.06$	ES-PIM $\alpha = 0.07$	ES-PIM $\alpha = 0.08$	ES-PIM $\alpha = 0.09$	ES-PIM $\alpha = 0.10$	ES-PIM $\alpha = 0.15$	FEM
2	5.825	5.657	5.502	5.358	5.223	5.095	4.552	4.960
3	4.341	4.294	4.249	4.206	4.163	4.122	3.930	4.097
4	4.285	4.241	4.200	4.159	4.120	4.082	3.904	4.091
5	3.729	3.714	3.701	3.687	3.673	3.660	3.595	3.713
6	3.637	3.627	3.618	3.608	3.599	3.590	3.544	3.653
7	3.587	3.580	3.573	3.566	3.559	3.553	3.519	3.614
8	3.555	3.549	3.544	3.539	3.534	3.529	3.503	3.575
9	3.550	3.545	3.540	3.535	3.531	3.526	3.502	3.568
10	3.529	3.525	3.521	3.518	3.514	3.510	3.491	3.547
15	3.476	3.475	3.474	3.472	3.471	3.470	3.463	3.489
20	3.463	3.462	3.461	3.461	3.460	3.459	3.456	3.471
30	3.453	3.453	3.453	3.452	3.452	3.452	3.450	3.457
40	3.450	3.450	3.450	3.449	3.449	3.449	3.449	3.452

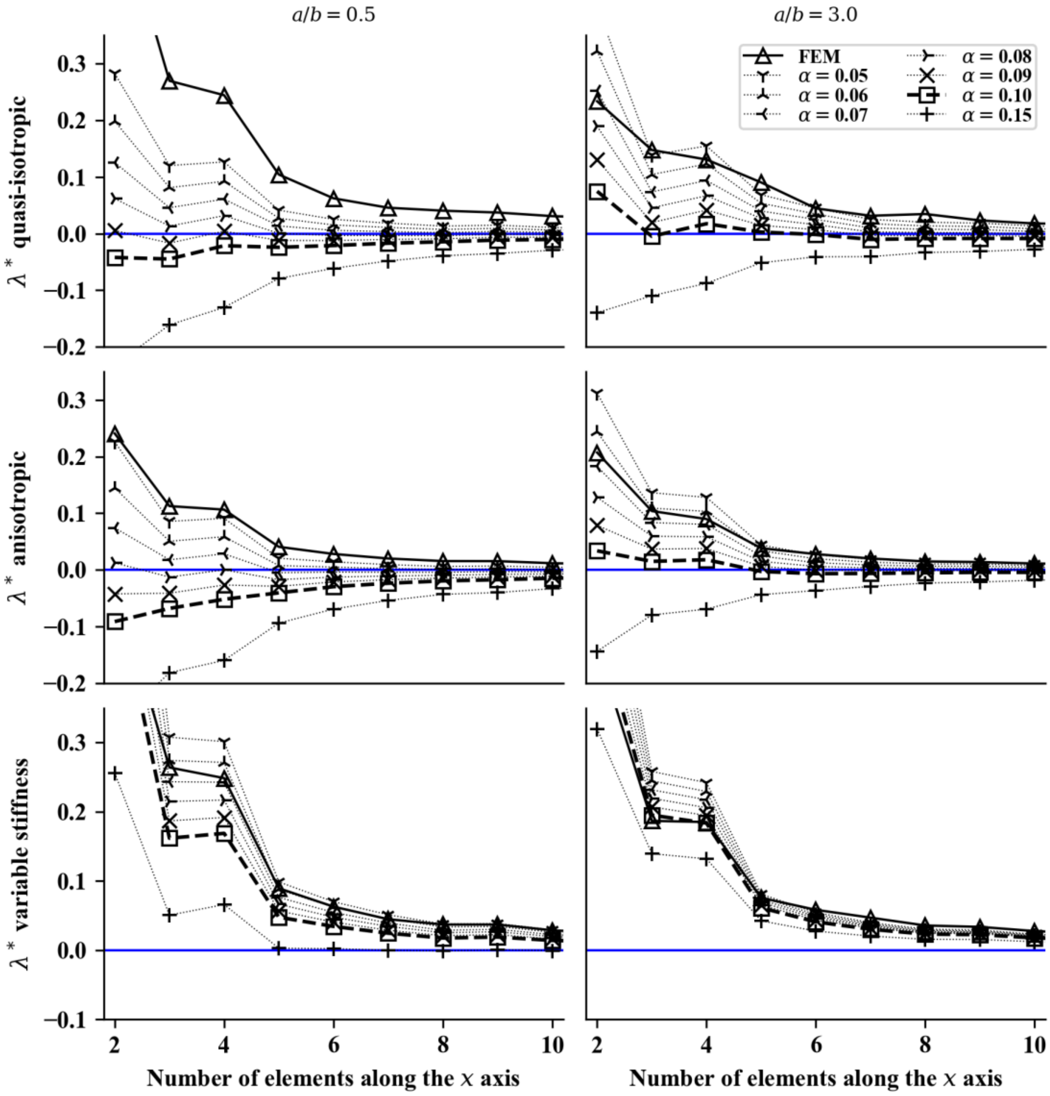

Fig. 13: Normalized 1^{st} eigenvalue, λ^{*}

6. Distorted Meshes

The mesh distortion will follow the procedure suggested by Liu [2] by altering the coordinates of the regular nodes using a prescribed irregularity factor α_{ir} ranging from 0.0 to 0.5:

$$\begin{aligned} x_{ir} &= x + \Delta x \cdot r_c \cdot \alpha_{ir} \\ y_{ir} &= y + \Delta y \cdot r_c \cdot \alpha_{ir} \end{aligned} \tag{38}$$

where Δx and Δy are respectively the initial regular nodal spacing in x- and y- directions; r_c a random number between -1.0 and$+1.0$. Fig. 14 shows two levels of mesh distortion using the same seed for the random numbers. In Table 9 it is shown the ES-PIM and FEM results, both quite insensitive to different mesh distortion levels.

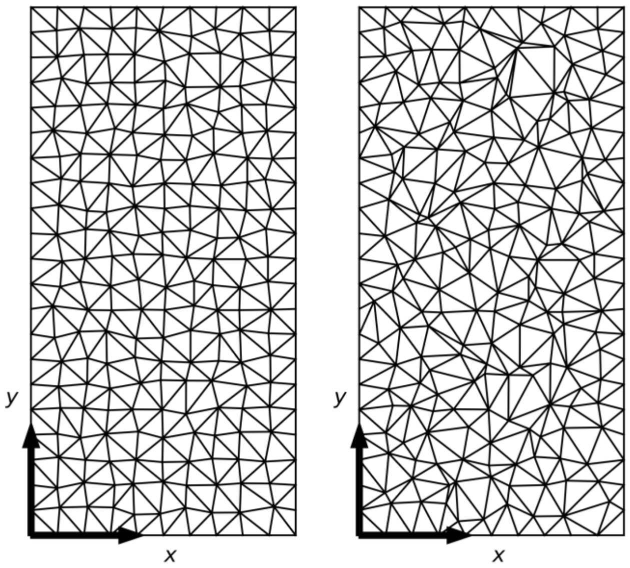

$\alpha_{ir} = 0.2$ $\alpha_{ir} = 0.5$

Fig. 14: Distorted meshes with 10 elements along x

Table 9 – Results for distorted mesh, ES-PIM with $\alpha = 0.08$, $a/b = 3.0$, 40 elements along x

α_{ir}	Quasi Isotropic		Anisotropic		Variable stiffness	
	ES	FEM	ES	FEM	ES	FEM
0.1	332.57	333.09	152.35	150.11	3.45	3.45
0.2	332.60	333.09	152.24	150.16	3.45	3.45
0.3	332.62	333.09	152.21	150.21	3.45	3.45
0.4	332.63	333.10	152.27	150.27	3.45	3.45
0.5	332.64	333.12	152.43	150.30	3.45	3.45

7. Conclusions

A formulation for linear buckling based on Mindlin–Reissner plate theory was develop in the context of the ES-PIM. It was shown how the geometric stiffness matrix can be calculated based on smoothed strains, where the pre-buckling membrane stresses successfully computed using constant smoothed strains within each integration cell, obtained from a previous static analysis result. The ES-PIM meshless method was successfully applied to predict linear buckling of variable tow (VAT) laminates. The proposed weighted average based on a nodal distribution of the constitutive properties led to slightly superior convergence rates than those achieved using NX Nastran`s CTRIA3. For the anisotropic and quasi-isotropic plates herein investigated, the observed convergence rates of the ES-PIM were even more pronounced.
The shear correction strategy proposed by Lyly et al. [34] was adopted, making it possible to investigate the influence of the α parameter on the convergence behavior of the ES-PIM for linear buckling. As previously observed by Bischoff and Bletzinger [45], high values of α ($\alpha > 0.09$ in the present study) can lead to overly soft behavior, whereas small values of α ($\alpha < 0.07$ in the present study) can lead to a delayed convergence. Interestingly, for $\alpha > 0.09$ a convergence from below was observed for linear buckling, which can be used within a preliminary design framework for conservative estimates of linear buckling load for VAT laminates.
Future research should focus on formulating the ES-PIM for geometrically nonlinear postbuckling analysis; application of the ES-PIM for shells, preferentially using higher order interpolation functions for the strain smoothing, especially aiming a better discretization of curved shell domains; enhanced shear correction factors to reduce the dependency of the parameter α; investigation of the node-based smoothed point interpolation method (NS-PIM) for linear buckling analysis; and application cases using global meshes with a relatively coarse mesh size with the ES-PIM estimating conservative critical buckling loads. Moreover, the authors believe that the strain smoothing techniques herein investigated provide a powerful method that should be further considered in other areas of continuum mechanics.
The code develop for the present investigation has been made available to the public domain [52].

8. Acknowledgments

To the free software communities that have provided convenient packages for the Python programming language: the Matplotlib [53] community with a complete plotting library; the SciPy and NumPy communities that have provided Python modules for scientific and numeric analysis [54]; the SymPy [55] community that has provided Python modules for symbolic manipulation.

9. References

[1] Zeng W, Liu GR. Smoothed Finite Element Methods (S-FEM): An Overview and Recent Developments. Arch Comput Methods Eng 2016;25:1–39. doi:10.1007/s11831-016-9202-3.

[2] Liu G, Karamanlidis D. Mesh Free Methods: Moving Beyond the Finite Element Method. vol. 56. 2003. doi:10.1115/1.1553432.

[3] Wahid H, Ahmad S, Nor MAM, Rashid MA. Prestasi kecekapan pengurusan kewangan dan agihan zakat: perbandingan antara majlis agama islam negeri di Malaysia. vol. 51. Chapman and Hall/CRC; 2017. doi:10.1017/CBO9781107415324.004.

[4] Chen JS, Wu CT, Belytschko T. Regularization of material instabilities by meshfree approximations with intrinsic length scales. Int J Numer Methods Eng 2000;47:1303–22. doi:10.1002/(SICI)1097-0207(20000310)47:7<1303::AID-NME826>3.0.CO;2-5.

[5] Liu GR, Dai KY, Nguyen TT. A smoothed finite element method for mechanics problems. Comput Mech 2007;39:859–77. doi:10.1007/s00466-006-0075-4.

[6] LIU GR. a Generalized Gradient Smoothing Technique and the Smoothed Bilinear Form for Galerkin Formulation of a Wide Class of Computational Methods. Int J Comput Methods 2008;05:199–236. doi:10.1142/S0219876208001510.

[7] Natarajan S, Ferreira AJM, Bordas SPA, Carrera E, Cinefra M. Analysis of composite plates by a unified formulation-cell based smoothed finite element method and field consistent elements. Compos Struct 2013;105:75–81. doi:10.1016/j.compstruct.2013.04.040.

[8] Nguyen-Thoi T, Phung-Van P, Nguyen-Xuan H, Thai-Hoang C. A cell-based smoothed discrete shear gap method using triangular elements for static and free vibration analyses of Reissner-Mindlin plates. Int J Numer Methods Eng 2012;91:705–41. doi:10.1002/nme.4289.

[9] Wu F, Liu GR, Li GY, Cheng AG, He ZC. A new hybrid smoothed FEM for static and free vibration analyses of Reissner-Mindlin Plates. Comput Mech 2014;54:865–90. doi:10.1007/s00466-014-1039-8.

[10] Nguyen-Xuan H, Rabczuk T, Nguyen-Thanh N, Nguyen-Thoi T, Bordas S. A node-based smoothed finite element method with stabilized discrete shear gap technique for analysis of Reissner-Mindlin plates. Comput Mech 2010;46:679–701. doi:10.1007/s00466-010-0509-x.

[11] Nguyen-Xuan H, Tran L V., Nguyen-Thoi T, Vu-Do HC. Analysis of functionally graded plates using an edge-based smoothed finite element method. Compos Struct 2011;93:3019–39. doi:10.1016/j.compstruct.2011.04.028.

[12] Nguyen-Xuan H, Tran L V., Thai CH, Nguyen-Thoi T. Analysis of functionally graded plates by an efficient finite element method with node-based strain smoothing. Thin-Walled Struct 2012;54:1–18. doi:10.1016/j.tws.2012.01.013.

[13] Nguyen-Quang K, Dang-Trung H, Ho-Huu V, Luong-Van H, Nguyen-Thoi T. Analysis and control of FGM plates integrated with piezoelectric sensors and actuators using cell-based smoothed discrete shear gap method (CS-DSG3). Compos Struct 2017;165:115–29. doi:10.1016/j.compstruct.2017.01.006.

[14] Ho-Huu V, Do-Thi TD, Dang-Trung H, Vo-Duy T, Nguyen-Thoi T. Optimization of laminated composite plates for maximizing buckling load using improved differential evolution and smoothed finite element method. Compos Struct 2016;146:132–47. doi:10.1016/j.compstruct.2016.03.016.

[15] Herath MT, Natarajan S, Prusty BG, St. John N. Smoothed finite element and genetic algorithm based optimization for shape adaptive composite marine propellers. Compos Struct 2014;109:189–97. doi:10.1016/j.compstruct.2013.10.016.

[16] Le-Anh L, Nguyen-Thoi T, Ho-Huu V, Dang-Trung H, Bui-Xuan T. Static and frequency optimization of folded laminated composite plates using an adjusted Differential Evolution algorithm and a smoothed triangular plate element. Compos Struct 2015;127:382–94. doi:10.1016/j.compstruct.2015.02.069.

[17] Yamanaka T, Heidari-Rarani M, Lessard L, Feret V, Hubert P. A new finite element method for modeling delamination propagation without additional degrees of freedom. Compos Struct 2016;147:82–98. doi:10.1016/j.compstruct.2016.03.040.

[18] Xu J, Lee CK, Tan KH. An XFEM frame for plate elements in yield line analyses. Int J Numer Methods Eng 2013;96:150–75. doi:10.1002/nme.4535.

[19] Liu GR. on G Space Theory. Int J Comput Methods 2009;06:257–89. doi:10.1142/S0219876209001863.

[20] Liu GR, Zhang GY. a Normed G Space and Weakened Weak (W 2) Interpolation Method. Int J Comput Methods 2009;6:147–79. doi:10.1142/S0219876209001796.

[21] Wu SC, Liu GR, Cui XY, Nguyen TT, Zhang GY. An edge-based smoothed point interpolation method (ES-PIM) for heat transfer analysis of rapid manufacturing system. Int J Heat Mass Transf 2010;53:1938–50. doi:10.1016/j.ijheatmasstransfer.2009.12.062.

[22] He ZC, Li GY, Zhong ZH, Cheng AG, Zhang GY, Liu GR, et al. An edge-based smoothed tetrahedron finite element method (ES-T-FEM) for 3D static and dynamic problems. Comput Mech 2013;52:221–36. doi:10.1007/s00466-012-0809-4.

[23] Phung-Van P, Nguyen-Thoi T, Le-Dinh T, Nguyen-Xuan H. Static and free vibration analyses and dynamic control of composite plates integrated with piezoelectric sensors and actuators by the cell-based smoothed discrete shear gap method (CS-FEM-DSG3). Smart Mater Struct 2013;22:95026. doi:10.1088/0964-1726/22/9/095026.

[24] LIU GR, ZHANG GY. a Novel Scheme of Strain-Constructed Point Interpolation Method for Static and Dynamic Mechanics Problems. Int J Appl Mech 2009;01:233–58. doi:10.1142/S1758825109000083.

[25] Zhang ZB, Wu SC, Liu GR, Chen WL. Nonlinear transient heat transfer problems using the meshfree ES-PIM. Int J Nonlinear Sci Numer Simul 2010;11.

[26] XUE BY, WU SC, ZHANG WH, LIU GR. a Smoothed Fem (S-Fem) for Heat Transfer Problems. Int J Comput Methods 2013;10:1340001. doi:10.1142/S021987621340001X.

[27] Raju G, White S, Wu Z, Weaver P. Optimal Postbuckling Design of Variable Angle Tow Composites using Lamination Parameters. 56th AIAA/ASCE/AHS/ASC Struct. Struct. Dyn. Mater. Conf., 2015. doi:10.2514/6.2015-0451.

[28] Wu Z, Raju G, Weaver PM. Optimization of postbuckling behaviour of variable thickness composite panels with variable angle tows: Towards "Buckle-Free" design concept. Int J Solids Struct 2017. doi:10.1016/j.ijsolstr.2017.08.037.

[29] Haldar A, Jansen EL, Rolfes R, Weaver PM. Tailoring snap-through loads in variable stiffness composites. AIAA/ASCE/AHS/ASC Struct Struct Dyn Mater Conf 2018 2018:1–14. doi:10.2514/6.2018-2245.

[30] Telford R, Peeters D, Oliveri V, Zucco G, Jones D, O'Higgins R, et al. Enhanced buckling performance of a stiffened, variable angle tow thermoplastic composite panel. AIAA/ASCE/AHS/ASC Struct Struct Dyn Mater Conf 2018 2018:1–14. doi:10.2514/6.2018-0480.

[31] Madeo A, Groh RMJ, Zucco G, Weaver PM, Zagari G, Zinno R. Post-buckling analysis of variable-angle tow composite plates using Koiter's approach and the finite element method. Thin-Walled Struct 2017;110:1–13. doi:10.1016/j.tws.2016.10.012.

[32] Bletzinger KU, Bischoff M, Ramm E. Unified approach for shear-locking-free triangular and rectangular shell finite elements. Comput Struct 2000;75:321–34. doi:10.1016/S0045-7949(99)00140-6.

[33] Phung-Van P, Nguyen-Thoi T, Le-Dinh T, Nguyen-Xuan H, Nguyen-Xuan PP-V and TN-T and TL-D and H. Static, free vibration analyses and dynamic control of composite plates integrated with piezoelectric sensors and actuators by the cell-based smoothed discrete shear gap method (CS-FEM-DSG3). Smart Mater Struct 2013;22:95026. doi:10.1088/0964-1726/22/9/095026.

[34] Lyly M, Stenberg R, Vihinen T. A stable bilinear element for the Reissner-Mindlin plate model. Comput Methods Appl Mech Eng 1993;110:343–57. doi:10.1016/0045-7825(93)90214-I.

[35] Siemens Industry Software. Element Library Reference. Siemens; 2014.

[36] Shadmehri F, Hoa S V., Hojjati M. Buckling of conical composite shells. Compos Struct 2012;94:787–92. doi:10.1016/j.compstruct.2011.09.016.

[37] Castro SGP, Mittelstedt C, Monteiro FAC, Arbelo MA, Ziegmann G, Degenhardt R. Linear buckling predictions of unstiffened laminated composite cylinders and cones under various loading and boundary conditions using semi-analytical models. Compos Struct 2014;118:303–15. doi:10.1016/j.compstruct.2014.07.037.

[38] Mindlin RD. Influence of Rotatory Inertia and Shear on Flexural Motions of Isotropic, Elastic Plates. J Appl Mech Asme 1951;18:31–8. doi:no doi.

[39] Musa NW. Elastic Bending Deformation of the Drill Strings in Channels of Curve Wells. Mod Mech Eng 2017;07:1–7. doi:10.4236/mme.2017.71001.

[40] Altenbach H. Book Review: *J. N. Reddy, Theory and Analysis of Elastic Plates and Shells*. vol. 88. 2008. doi:10.1002/zamm.200890020.

[41] Guz' AN, Guz' G V. Mechanics of composite materials with large-scale curving of filler. Mech Compos Mater 1983;18:434–9. doi:10.1007/BF00611782.

[42] Arfken GB, Weber HJ, Spector D. *Mathematical Methods for Physicists, 4th ed* . vol. 67. 1999. doi:10.1119/1.19217.

[43] Budiansky B. Theory of Buckling and Post-Buckling Behavior of Elastic Structures. Adv. Appl. Mech., 1974, p. 1–65. doi:10.1016/S0065-2156(08)70030-9.

[44] Castro SGP. Semi-Analytical Tools for the Analysis of Laminated Composite Cylindrical and Conical Imperfect Shells under Various Loading and Boundary Conditions. Clausthal University of Technology, 2014. doi:10.21268/20150210-154320.

[45] Bischoff M, Bletzinger KU. Improving stability and accuracy of Reissner-Mindlin plate finite elements via algebraic subgrid scale stabilization. Comput Methods Appl Mech Eng 2004;193:1517–28. doi:10.1016/j.cma.2003.12.036.

[46] Vlachoutsis S. Shear correction factors for plates and shells. Int J Numer Methods Eng 1992;33:1537–52. doi:10.1002/nme.1620330712.

[47] Kim BC, Weaver PM, Potter K. Manufacturing characteristics of the continuous tow shearing method for manufacturing of variable angle tow composites. Compos Part A Appl Sci Manuf 2014;61:141–51. doi:10.1016/j.compositesa.2014.02.019.

[48] Blom AW, Stickler PB, Gürdal Z. Optimization of a composite cylinder under bending by tailoring stiffness properties in circumferential direction. Compos Part B Eng 2010;41:157–65. doi:10.1016/j.compositesb.2009.10.004.

[49] Wu Z, Weaver PM, Raju G. Postbuckling optimisation of variable angle tow composite plates. Compos Struct 2013;103:34–42. doi:10.1016/j.compstruct.2013.03.004.

[50] Groh RMJ, Weaver PM. Buckling analysis of variable angle tow, variable thickness panels with transverse shear effects. Compos Struct 2014;107:482–93. doi:10.1016/j.compstruct.2013.08.025.

[51] Leissa AW. Conditions for laminated plates to remain flat under inplane loading. Compos Struct 1986;6:261–70. doi:10.1016/0263-8223(86)90022-X.

[52] Castro SGP. Meshless Methods for Computational Mechanics, Version 0.1.26. Available online at https://github.com/compmech/meshless 2018.

[53] Hunter JD. Matplotlib: A 2D graphics environment. Comput Sci Eng 2007;9:99–104. doi:10.1109/MCSE.2007.55.

[54] Oliphant TE. Python for scientific computing. Comput Sci Eng 2007;9:10–20. doi:10.1109/MCSE.2007.58.

[55] Meurer A, Smith CP, Paprocki M, Čertík O, Kirpichev SB, Rocklin M, et al. SymPy: symbolic computing in Python. PeerJ Comput Sci 2017;3:e103. doi:10.7717/peerj-cs.103.